

Article

Phase Transformation by 100 keV Electron Irradiation in Partially Stabilized Zirconia

Yasuki Okuno ^{1,*} and Nariaki Okubo ²¹ KINKEN, Tohoku University, 2-1 Katahira, Aoba-ku, Sendai City 980-8577, Miyagi, Japan² Japan Atomic Energy Agency, 2-4 Shirakata, Tokai-Mura 319-1195, Ibaraki-Ken, Japan; okubo.nariaki@jaea.go.jp

* Correspondence: okuno.yasuki@imr.tohoku.ac.jp; Tel.: +81-022-215-2068

Abstract: Partially stabilized zirconia (PSZ) is considered for use as an oxygen-sensor material in liquid lead-bismuth eutectic (LBE) alloys in the radiation environment of an acceleration-driven system (ADS). To predict its lifetime for operating in an ADS, the effects of radiation on the PSZ were clarified in this study. A tetragonal PSZ was irradiated with 100 keV electrons and analyzed by X-ray diffraction (XRD). The results indicate that the phase transition in the PSZ, from the tetragonal to the monoclinic phase, was caused after the irradiation. The deposition energy of the lattice and the deposition energy for the displacement damage of a 100 keV electron in the PSZ are estimated using the particle and heavy ion transport code system and the non-ionizing energy loss, respectively. The results suggest that conventional radiation effects, such as stopping power, are not the main mechanism behind the phase transition. The phase transition is known to be caused by the low-temperature degradation of the PSZ and is attributed to the shift of oxygen ions to oxygen sites. When the electron beam is incident to the material, the kinetic energy deposition and excitation-related processes are caused, and it is suggested to be a factor of the phase transition.



Citation: Okuno, Y.; Okubo, N. Phase Transformation by 100 keV Electron Irradiation in Partially Stabilized Zirconia. *Quantum Beam Sci.* **2021**, *5*, 20. <https://doi.org/10.3390/qubs5030020>

Academic Editors: Akihiro Iwase and Rozaliya Barabash

Received: 5 April 2021
Accepted: 11 June 2021
Published: 25 June 2021

Publisher's Note: MDPI stays neutral with regard to jurisdictional claims in published maps and institutional affiliations.



Copyright: © 2021 by the authors. Licensee MDPI, Basel, Switzerland. This article is an open access article distributed under the terms and conditions of the Creative Commons Attribution (CC BY) license (<https://creativecommons.org/licenses/by/4.0/>).

Keywords: phase transition; electron irradiation; partially stabilized zirconia; XRD; radiation simulation

1. Introduction

An acceleration-driven system (ADS) is a powerful tool for effectively transmuted minor actinides in the double-strata fuel cycle strategy for separation/conversion technology [1,2]. As a neutron source and coolant, such systems use a liquid lead–bismuth eutectic (LBE) alloy as a nuclear spallation target [3]. The LBE alloy is designed to flow through piping at 2 m/s. It causes erosion and corrosion in the pipes [4,5], which are suppressed by adjusting the oxygen concentration by about 10^{−7} wt.% in the LBE alloy [6]. Therefore, an oxygen sensor is required to control the oxygen concentration in the LBE alloy.

Oxygen sensors based on yttria-stabilized zirconia (YSZ) and a Pt/air electrode are used worldwide to monitor the oxygen concentration in LBE alloys [7,8]. Such oxygen sensors must have high fracture toughness because a high load is applied by the flowing LBE alloy. The fracture toughness of YSZ depends on the yttrium concentration [9]. YSZ with 3 mol% yttrium is called partially stabilized zirconia (3Y-PSZ).

Under high stress, 3Y-PSZ undergoes a phase transition from a tetragonal (t) phase to a monoclinic (m) phase [10–12]. Because the m phase contributes to arresting crack propagation, it has been shown to play an important role in endowing this material with high fracture toughness. Therefore, if the fracture toughness can be maintained in the ADS operating environment, the PSZ may become an important material for use in ADS oxygen sensors.

As the LBE alloy flows through the entire ADS cooling system, it becomes radioactive through the spallation reaction. The LBE alloy is predicted to expose the oxygen sensor to a high radiation field of over 1 kGy/h [6], which is expected to lead to radiation damage in the oxygen-sensor material.

In a previous study of pure zirconia irradiated with 340 keV Xe and 800 keV Bi ion beams [13–15], an m-to-t phase transition was observed. The phase transition between m and t is considered to be caused by the cumulative transfer of energy laid down in the displacement cascades. On the other hand, the t phase of 3Y-PSZ is a metastable phase and is related to its strong mechanical properties. However, the t-to-m transition is triggered by mechanical stress and thermal annealing, and may be affected by the deposition energy of the radiation because of the metastable state phase.

To use the PSZ device in a radiation environment, the behavior of the PSZ in the metastable t phase must be investigated. In this study, the effect of PSZ on a 100 keV electron beam was investigated, using a crystal structure and radiation simulation analysis.

2. Materials and Methods

The PSZ specimens consisted of zirconia doped with 3 mol% yttria (3Y-PSZ, Tsukuba Ceramic Works) and were cut into 4.0 mm (length) \times 10.0 mm (width) \times 3.0 mm (depth) specimens. They were sintered at 1500 °C. The top and bottom surfaces were mirror polished. To remove the phase transition during the shape processing, the PSZ specimens were processed with a quench heat treatment at 900 °C and air cooled.

The specimens were irradiated with a 100 keV electron beam generated by a Cockcroft–Walton electron accelerator at Osaka Prefecture University (OPU). In order to avoid generating heat in a small area with the micro-focus beam, the electron beam was defocused to about 2 cm Φ . The area of irradiation was extended to 6 cm \times 10 cm much more than the surface of the sample by the scanning coil. The required electron fluence was determined from the number of charges flowing to the ground collected in a Faraday cup and the flux was 5×10^{12} cm²/s during the irradiation. Before and after irradiation, the specimens were subjected to X-ray diffraction (XRD), and the crystal structure was analyzed using the θ – 2θ method. The XRD measurements were carried out using Cu K α radiation.

3. Results

Figure 1 shows the XRD pattern of 3Y-PSZ before and after irradiation with a 100 keV electron beam. In Figure 1a, the main XRD peaks are assigned to all measurement regions. This result indicates that the t (111) phase dominates the 3Y-PSZ specimen at approximately $2\theta = 30^\circ$, before and after irradiation [16]. The peaks of the m (11 – 1) and (111) phases at approximately $2\theta = 28^\circ$ and 31.5° do not appear because the signal intensity is much lower than that of the t phase. A peak is known to exist in the m (11 – 1) phase.

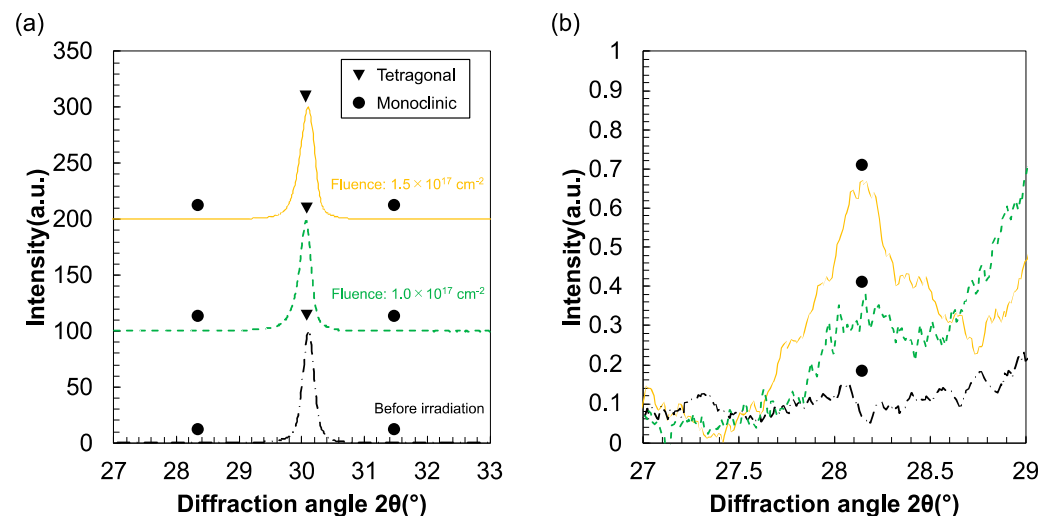


Figure 1. XRD patterns of a PSZ specimen before and after irradiation with 100 keV electron beams. The black line is before irradiation. (a) is the spectrum of the measured range shifted up by 100; (b) is the spectrum focused on m (11 – 1) between 27 and 29°.

In Figure 1b, to focus on the m (11 – 1) peak, the diffraction angle was set between 27° and 29°. The results show that the intensity of the peak monotonically increases after irradiation, depending on the fluence of 100 keV electrons.

The fraction C_M of the m phase to the t phase can be evaluated from the peak areas of the most intense signals of t (101), m (11 – 1), and t (111), using the following equation [13]:

$$C_M = 0.82 \times \frac{I_m(11-1) + I_m(111)}{I_t(101)} \times 100\% \quad (1)$$

where I_m and I_t are the peak intensities of m and t, respectively. Figure 2 shows the fractional content of the m phase as a function of the electron fluence. This result indicates that the fractional content of m increases as the absorbed dose increases. Therefore, the phase transformation in 3Y-PSZ is caused by electron irradiation.

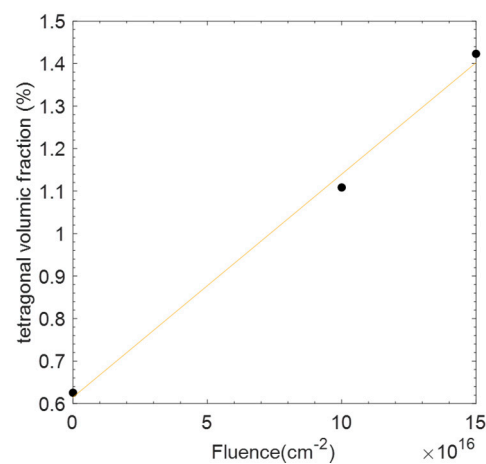


Figure 2. Fraction of monoclinic zirconia as a function of the fluence of 100 keV electrons.

Because the phase transition is detected by XRD, the absorbed dose should be calculated in the shallow surface region that is probed by XRD. This region was determined by the X-ray penetration depth. The fraction $G(x)$ of the total diffracted intensity, due to a surface layer of depth xx , can be expressed using the following [17,18]:

$$G(x) = 1 - \exp\left(\frac{-2\mu x}{\sin \theta}\right) \quad (2)$$

where μ is the absorption coefficient and $-2\mu x / \sin \theta$ is the effective path length for X-rays to penetrate to a depth x at a given Bragg angle θ . For the PSZ, the path length of Cu $K\alpha$ X-rays incident at $\theta = 28^\circ$ is approximately 9 μm , as shown in Equation (2), with $G(x) = 0.99$. The electrons are known to have a short flight distance in the materials. To investigate the range of the flight distance, the Monte Carlo calculation for radiation behavior was conducted, using the particle and heavy ion transport code system (PHITS) [19].

Figure 3 shows the depth distribution of the dose from the surface of the PSZ, in the case of irradiation with one of the 100 keV electrons. This result indicates that the value of the dose rate peaks at approximately 5 μm , and continues to 30 μm . Therefore, the flight range of a 100 keV electron was considered to be longer than the observation range of the XRD analysis.

When charged particles, e.g., electrons and ions, pass through materials, the radiation effect is expressed as a loss of energy, due to an interaction called total stopping power (S). One type of S is collision stopping power (S_{col}), e.g., electronic stopping power (S_e), nuclear stopping power (S_n), and radiative stopping power (S_{rad}). S_n is the main factor that causes the displacement and migration of atoms.

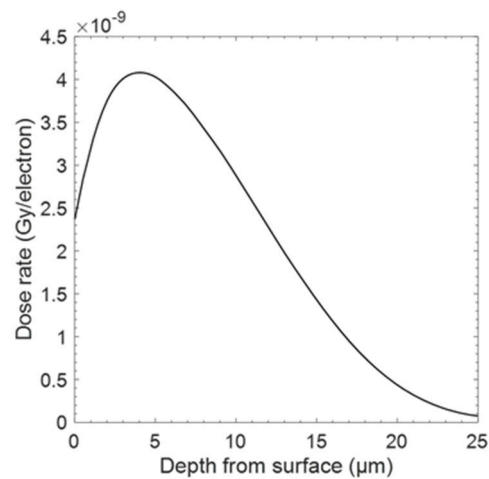


Figure 3. Calculation result of dose rate as a function of the depth from surface.

In an effort to describe the fraction of energy that moves into displacements such as the S_n , due to radiation, the non-ionizing energy loss (NIEL) was developed and is expressed as follows [20–22]:

$$\text{NIEL}(E) = \frac{N_A}{A} \int_{\theta_{\min}}^{\pi} L[T(\theta, E)] T(\theta, E) \frac{d\sigma(\theta, E)}{d\Omega} d\Omega \quad (3)$$

where N_A is Avogadro's number, A is the atomic mass, E is the energy of the incident particle, θ is the scattering angle, σ is the scattering cross-section, and Ω is the solid angle of scattering. The equation also requires information regarding the differential cross-section for atomic displacements ($d\sigma(\theta, E)/d\Omega$), the average recoil energy of the target atoms ($T(\theta, E)$), and the Lindhard partition factor ($L[T(\theta, E)]$), which partitions the energy into ionizing and non-ionizing events.

Figure 4 shows the NIEL vs. energy for Zr, Y, and O atoms for electrons. The result shows that the NIEL value for each element rapidly increases above a certain energy threshold (E_{th}). An increase in the NIEL value means that the kinetic energy given by the electron beam to the atom exceeds the displacement threshold energy (E_d) and causes the production of a primary knock-on atom (PKA).

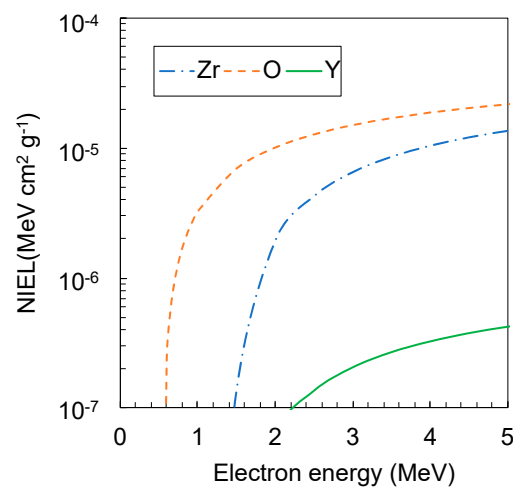


Figure 4. Non-ionizing energy loss (NIEL) vs. electron energy calculated for Zr, Y, and O atoms. The values of E_d for Zr, Y, and O are 80, 80, and 120 eV, respectively.

However, the E_{th} values of Y, Zr, and O are higher than the energy of the incident electrons by approximately 2200, 1250, and 600 keV, respectively. Therefore, the phase

transition is considered to be caused by the transfer of kinetic energy lower than the recoil effect, similar to PKA.

From the calculation result in Figure 3, the deposition energy such as the S_e is also estimated to be 1.9×10^{-14} eV when an electron passes the lattice of t-PSZ having a volume of 137 \AA^3 , which might be much lower than the energy that causes the phase transition.

The phase transition from t to m in the PSZ is also known to be a thermal effect which is between 150 and 300 °C, as shown in Figure 5 [23]. The electron beam that heats the sample surface is considered to be about 80 mW because the condition of electron beam is a defocus-beam, rather than a micro-focus beam. The region such as 25 μm from the surface, which is main energy deposition region indicated from Figure 3, is 11 K/s. The sample temperature between the electron irradiation was less than 40 °C. For the above reasons, in the irradiation, the sample temperature is lower than the annealing temperature which causes a phase transition from the t-to-m phase. Therefore, the observed phase transition caused by the irradiation with 100 keV electrons is not considered to be a radiation effect such as the S_e , the S_n and the thermal effect.

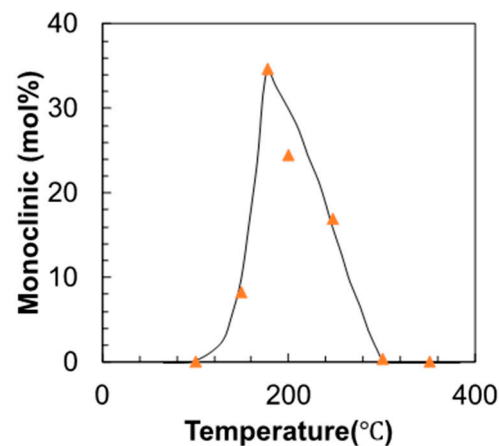


Figure 5. Relationship between the amount of the monoclinic phase and annealing temperature in PSZ fabricated above 1500 °C [23]. The annealing time is 50 h.

4. Discussion

The crystal structures of the t and m phases of PSZ are shown in Figure 6 [24]. This phase transformation is considered to be a martensitic transition. Generally, an athermal diffusionless martensitic transition occurs quickly, with the motion of the phase boundary as high as the speed of sound [25]. The overall transition proceeds in two major stages [26]. First, the transition of the lattice structure from tetragonal to monoclinic occurs by the shearing displacement of zirconium ions. The second stage involves the sliding of oxygen ions to the oxygen sites in the monoclinic lattice. The displacement of oxygen ions from the ideal fluorite positions along the c-axis was investigated by X-ray diffraction (XRD) [27]. Therefore, the 100 keV electron is considered to cause the shearing displacement of zirconium ions and the sliding of oxygen ions. In [9], the reported activation energies for the phase transition are close to 100 kJ/mol (~1 eV), which is similar to the activation energy for the sliding of oxygen ions to oxygen sites. In order to find the mechanism of the phase transition, the factor of the sliding of oxygen ions to oxygen sites should be considered.

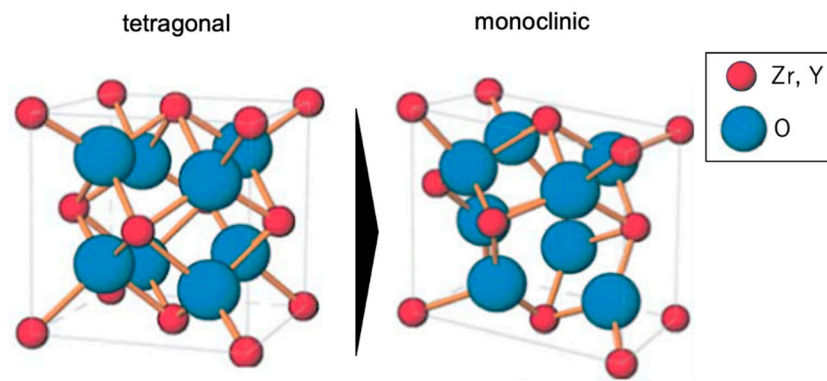


Figure 6. Crystal structure of monoclinic and tetragonal partially stabilized zirconia [24].

One of the factors is the kinetic energy transfer due to the elastic collision between the electron and target atoms. The kinetic energy of the target atom from the incident electron is expressed as follows:

$$E_p = \frac{2M_e}{M_T} \cdot \frac{1}{M_e c^2} (E + 2M_e c^2) E \sin^2 \frac{\theta}{2} \quad (4)$$

where E , θ , c , M_T , and M_e denote the energy of the incident electron, scattering angle, speed of light, mass of the target atom, and electron mass, respectively. Therefore, in the case of $\theta = 0^\circ$, E_p takes the maximum value ($E_{p,max}$), which is represented by the following equation:

$$E_{p,max} = \frac{2E(E + 2M_e c^2)}{M_T c^2} \quad (5)$$

Figure 7 shows the $E_{p,max}$ for Zr, Y, and O atoms, as a function of the energy of the incident electron. The result shows that the value of $E_{p,max}$ for the O atom is 1 eV at the energy of the 7.2 keV incident electron. This suggests that a 100 keV electron can cause the migration of oxygen ions to oxygen sites, by elastic scattering, to trigger the phase transition.

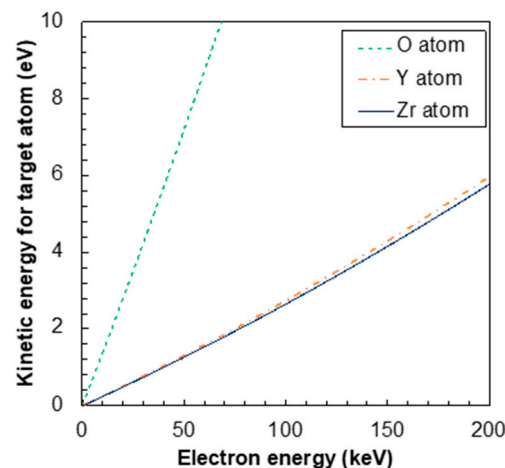


Figure 7. Kinetic energy transfer for Zr, Y, and O atoms due to elastic scattering as a function of the energy of the incident electron.

Another factor to consider are the excitation-related processes [28]. The amorphous-to-crystalline phase transition via the excitation-related processes is often observed in amorphous ceramics such as Al_2O_3 , ScPO_4 and LaPO_4 [29]. The behavior of phase transi-

tion via excitation-related processes is known to have an approximate relationship with the Bethe formula [30], which is as the following:

$$-\frac{dE}{dx} = 2\pi e^4 N_A \frac{\rho Z}{AE} \ln\left(\sqrt{\frac{E}{2I}}\right) \quad (6)$$

$$I = 9.76\bar{Z} + \frac{58.5}{\bar{Z}^{0.19}}, \quad (7)$$

where e is the elementary charge, N_A is the Avogadro number, ρ is the mass density, Z is the atomic number, A is the atomic weight, E is the electron energy, \ln is the base of natural logarithm, I is the mean excitation energy, and \bar{Z} is the mean atomic number.

Figure 8 shows the calculation result of the stopping power for electron in ZrO_2 as a function of the energy of the incident electron. The result indicates that the stopping power increases with the decreasing incident electron energy. This tendency is in contrast to the kinetic energy of the elastic collision as shown in Figure 7. The possible factors that cause the phase transformation are the transfer of kinetic energy or the electronic excitation effect. In further research, in order to investigate the mechanism of the $m \rightarrow t$ phase transition in PSZ, it is important to determine the energy dependence of the phase transformation by low-energy electron beams. If the phase transformation rate increases with decreasing incident electron energy, the electronic excitation effect is the main factor. On the other hand, when the tendency between the energy and the phase transformation rate is opposite, the influence of kinetic energy application is considered to be large.

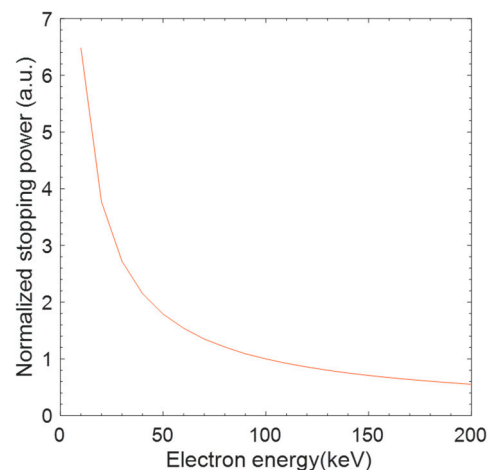


Figure 8. Stopping power for incident electrons normalized at 100 keV electron energy in ZrO_2 .

5. Conclusions

It was observed that the monoclinic phase in 3Y-PSZ increased with increasing electron-beam fluence. The calculation results using PHITS suggested that the energy deposited by a 100 keV electron to the PSZ lattice was not the main reason for the phase transition. The NIEL calculation indicated that the atoms in the PSZ only recoiled under electron irradiation at energies over 0.56 MeV; 100 keV electrons cannot cause displacement damage.

However, the kinetic energy or the excitation-related processes from incident electrons in the PSZ might be higher than the energy needed to shift oxygen ions to oxygen sites, and is suggested to be the cause of the phase transition.

Author Contributions: Conceptualization, Y.O. and Y.O.; methodology, Y.O.; software, Y.O.; validation, Y.O.; formal analysis, Y.O.; investigation, Y.O.; resources, N.O.; data curation, Y.O.; writing—original draft preparation, Y.O.; writing—review and editing, Y.O.; visualization, Y.O.; supervision, N.O.; project administration, N.O.; funding acquisition, N.O. All authors have read and agreed to the published version of the manuscript.

Funding: This research received no external funding.

Acknowledgments: We would like to thank Takashi Oka and Shuichi Okuda (OPU) for supporting our electron irradiation tests.

Conflicts of Interest: The authors declare no conflict of interest.

References

1. Tsujimoto, K.; Oigawa, H.; Ouchi, N.; Kikuchi, K.; Kurata, Y.; Mizumoto, M.; Sasa, T.; Saito, S.; Nishihara, K.; Umeno, M.; et al. Research and Development Program on Accelerator Driven Subcritical System in JAEA. *J. Nucl. Sci. Technol.* **2007**, *44*, 483. [[CrossRef](#)]
2. Oigawa, H.; Tsujimoto, K.; Nishihara, K.; Sugawara, T.; Kurata, Y.; Takei, H.; Saito, S.; Sasa, T.; Obayashi, H. Role of ADS in the back-end of the fuel cycle strategies and associated design activities: The case of Japan. *J. Nucl. Mater.* **2011**, *415*, 229. [[CrossRef](#)]
3. Kurata, Y. Corrosion experiments and materials developed for the Japanese HLM systems. *J. Nucl. Mater.* **2011**, *415*, 254. [[CrossRef](#)]
4. Yeliseyeva, O.; Tsisar, V.; Benamati, G. Influence of temperature on the interaction mode of T91 and AISI 316L steels with Pb–Bi melt saturated by oxygen. *Corros. Sci.* **2008**, *50*, 1672. [[CrossRef](#)]
5. Schroer, C.; Skrypnik, A.; Wedemeyer, O.; Konys, J. Oxidation and dissolution of iron in flowing lead–bismuth eutectic at 450 °C. *Corros. Sci.* **2012**, *61*, 63. [[CrossRef](#)]
6. Deloffre, P.; Terlain, A.; Barbier, F. Corrosion and deposition of ferrous alloys in molten lead–bismuth. *J. Nucl. Mater.* **2002**, *301*, 35–39. [[CrossRef](#)]
7. Fernandez, J.A.; Abella, J.; Barcelo, J.; Victori, L. Development of an oxygen sensor for molten 44.5% lead–55.5% bismuth alloy. *J. Nucl. Mater.* **2002**, *301*, 47–52. [[CrossRef](#)]
8. Schroer, C.; Konys, J.; Verdaguer, A.; Abella, J.; Gessi, A.; Kobzova, A.; Babayan, S.; Courouau, J.-L. Design and testing of electrochemical oxygen sensors for service in liquid lead alloys. *J. Nucl. Mater.* **2011**, *415*, 338–347. [[CrossRef](#)]
9. Chevalier, J.; Cremillard, L.; Virkar, A.V.; Clarke, D.R. The Tetragonal-Monoclinic Transformation in Zirconia: Lessons Learned and Future Trends. *J. Amer. Ceram. Soc.* **2009**, *92*, 1901–1920. [[CrossRef](#)]
10. Ramos, C.M.; Tabata, A.S.; Cesar, P.F.; Rubo, J.H.; Fracisconi, P.A.S.; Borges, A.F.S. Application of Micro-Raman Spectroscopy to the Study of Yttria-Stabilized Tetragonal Zirconia Polycrystal (Y-TZP) Phase Transformation. *Appl. Spectrosc.* **2015**, *69*, 810–814. [[CrossRef](#)]
11. Paul, A.; Vaidhyanathan, B.; Binner, J. Micro-Raman spectroscopy of indentation induced phase transformation in nanozirconia ceramics. *Adv. Appl. Ceram.* **2011**, *110*, 114–119. [[CrossRef](#)]
12. Melk, L.; Turon-Vinas, M.; Roa, J.J.; Antti, M.L.; Anglada, M. The influence of unshielded small cracks in the fracture toughness of yttria and of ceria stabilised zirconia. *J. Eur. Ceram. Soc.* **2016**, *36*, 147. [[CrossRef](#)]
13. Simeone, D.; Bechade, J.L.; Gosset, D.; Chevarier, A.; Daniel, P.; Pilliaire, H.; Baldinozzi, G. Investigation on the zirconia phase transition under irradiation. *J. Nucl. Mater.* **2000**, *281*, 171–181. [[CrossRef](#)]
14. Simeone, D.; Gosset, D.; Bechade, J.L.; Chevarier, A. Analysis of the monoclinic–tetragonal phase transition of zirconia under irradiation. *J. Nucl. Mater.* **2002**, *300*, 27–38. [[CrossRef](#)]
15. Simeone, D.; Baldinozzi, G.; Gosset, D.; Duthheil, M.; Bulou, A.; Hansen, T. Monoclinic to tetragonal semireconstructive phase transition of zirconia. *Phys. Rev. B* **2003**, *67*, 1–8. [[CrossRef](#)]
16. Leib, E.W.; Vainio, U.; Pasquarelli, R.M.; Kus, J.; Czaschke, C.; Walter, N.; Janssen, R.; Müller, M.; Schreyer, A.; Weller, H.; et al. Synthesis and thermal stability of zirconia and yttria-stabilized zirconia microspheres. *J. Colloid Interface Sci.* **2015**, *448*, 582. [[CrossRef](#)]
17. Ishikawa, N.; Sonoda, T.; Okamoto, Y.; Sawabe, T.; Takegahara, K.; Kosugi, S.; Iwase, A. X-ray Study of Radiation Damage in UO₂ Irradiated with High-Energy Heavy Ions. *J. Nucl. Mater.* **2011**, *419*, 392–396. [[CrossRef](#)]
18. Blanton, T.N.; Barnes, C.L.; Lelental, M. The effect of X-ray penetration depth on structural characterization of multiphase Bi-Sr-Ca-Cu-O thin films by X-ray diffraction techniques. *Phys. C* **1991**, *173*, 3–4. [[CrossRef](#)]
19. Sato, T.; Iwamoto, Y.; Hashimoto, S.; Ogawa, T.; Furuta, T.; Abe, S.; Kai, T.; Tsai, P.; Matsuda, N.; Iwase, H.; et al. Features of Particle and Heavy Ion Transport code System (PHITS) version 3.02. *J. Nucl. Sci. Technol.* **2018**, *55*, 684. [[CrossRef](#)]
20. Messenger, S.R.; Burke, E.A.; Xapsos, M.A.; Walters, R.J.; Jackson, E.M.; Weaver, B.D. Nonionizing Energy Loss (NIEL) for Heavy Ions. *IEEE Trans. Nucl. Sci.* **1999**, *46*, 1595. [[CrossRef](#)]
21. Jun, I.; Xapsos, M.A.; Messenger, S.R.; Burke, E.A.; Walters, R.J.; Summers, G.P.; Jordan, T. Proton nonionizing energy loss (NIEL) for device applications. *IEEE Trans. Nucl. Sci.* **2003**, *50*, 1924.
22. Summers, G.P.; Burke, E.A.; Xapsos, M.A. Displacement damage analogs to ionizing radiation effects. *Radiat. Meas.* **1995**, *24*, 1–8. [[CrossRef](#)]
23. Sato, T.; Ohtaki, S.; Shimada, M. Transformation of yttria partially stabilized zirconia by low temperature annealing in air. *J. Mater. Sci.* **1985**, *20*, 1466. [[CrossRef](#)]
24. Brog, J.P.; Chanez, A.C.; Crochet, A.; Fromm, K.M. Polymorphism, what it is and how to identify it: A systematic review. *RSC Adv.* **2013**, *3*, 16905. [[CrossRef](#)]

25. Cohen, M.; Wayman, C.M. Fundamentals of martensitic reactions. In *Metallurgical Treatises*; Tien, J.K., Elliott, J.F., Eds.; TMS-AIME: Warrendale, PA, USA, 1983; pp. 445–468.
26. Ge, Q.L.; Lei, T.C.; Mao, J.F.; Zhou, Y. In situ transmission electron microscopy observations of the tetragonal-to-monoclinic phase transformation of zirconia in Al₂O₃-ZrO₂ (2 mol % Y₂O₃) composite. *J. Mater. Sci. Lett.* **1993**, *12*, 819–822. [[CrossRef](#)]
27. Lamas, D.G.; Walsøe de Reca, N.E. Oxygen ion displacement in compositionally homogeneous, nanocrystalline ZrO₂-12 mol% Y₂O₃ powders. *Mater. Lett.* **1999**, *41*, 204–208. [[CrossRef](#)]
28. Nakamura, R.; Ishimaru, M.; Yasuda, H.; Nakajima, H. Atomic rearrangements in amorphous Al₂O₃ under electron-beam irradiation. *J. Appl. Phys.* **2013**, *113*, 064312. [[CrossRef](#)]
29. Meldrum, A.; Boatner, L.A.; Ewing, R.C. Electron-irradiation-induced nucleation and growth in amorphous LaPO₄, ScPO₄, and zircon. *J. Mater. Res.* **1997**, *12*, 1816. [[CrossRef](#)]
30. Nguyen-Truong, H.T. Modified Bethe formula for low-energy electron stopping power without fitting parameters. *Ultramicroscopy* **2015**, *149*, 26–33. [[CrossRef](#)] [[PubMed](#)]